Astron. Nachr. / AN **334**, No. 6, 499 – 514 (2013) / **DOI** 10.1002/asna.201311897

Cosmological simulations of galaxy formation: Successes and challenges in the era of supercomputers

Ludwig Biermann Award Lecture 2012

C. Scannapieco⋆

Leibniz-Institut für Astrophysik Potsdam (AIP), An der Sternwarte 16, D-14482 Potsdam, Germany

Received 2013 Jan 18, accepted 2013 Mar 22
Published online 2013 Jul 1

Key words cosmology: theory – galaxies: formation – galaxies: evolution – methods: numerical

I use cosmological hydrodynamical simulations to study the formation and evolution of galaxies similar in mass to the Milky Way. First, I use a set of eight simulations where the haloes have a great variety of merger and formation histories, to investigate how similar or diverse these galaxies are at the present epoch, and how their final properties are related to the particular formation history of the galaxy. I find that rotationally-supported disks are present in 7 of the 8 galaxies at $z \sim 2$–3; however, only half of the galaxies have significant disks at $z = 0$. Both major mergers and the accretion of gas that is misaligned with the preexisting stellar disk contribute to the transfer of material from the disks to the spheroidal components, lowering the disk-to-total ratios during evolution. I also present and discuss recent results of the Aquila Project, which compares the predictions of 13 different numerical codes for the properties of a galaxy in a Λ cold dark matter universe. All simulations use a unique initial condition and are analysed in the exact same way, allowing a fair comparison of results. We find large code-to-code variations in stellar masses, star formation rates, galaxy sizes and morphologies. We also find that the way feedback is implemented is the main cause of the differences, although some differences might also result from the use of different numerical technique. Our results show that state-of-the-art simulations cannot yet uniquely predict the properties of the baryonic component of a galaxy, even when the assembly history of its host halo is fully specified.

1 Introduction

Within the current cosmological paradigm, the Λ cold dark matter (ΛCDM) model, galaxies form as small density perturbations grow via gravitational instability and collapse, forming the seeds for future dark matter haloes. In this context, structure formation is a hierarchical process: small systems form first and larger systems form later via aggregation of matter and mergers. Within the haloes, gas cools down and can collapse further, eventually forming stars. If gas retains its angular momentum during collapse, the gas – and then the stars – will form a rotationally supported disk.

The galaxy formation process is extremely complex, highly non-linear and free from any simplifying symmetries. Furthermore, during evolution, dark matter haloes and the galaxies within them are continuously affected by accretion, interaction with satellites and merger events. Numerical simulations are the only possible way to follow such a complex evolution. However, due to the huge dynamical range that cosmological simulations need to cover, processes such as star formation and feedback cannot be included from first principles, and can only be added as subgrid physics.

Among the hydrodynamical processes that are included in simulations, supernova (SN) feedback has shown to be of particular importance. Early models only included gas cooling and star formation, and were unable to reproduce the formation of galaxy disks from cosmological initial conditions. The angular momentum problem, as it is called, occurs as baryons lose angular momentum during mergers and interactions, and the resulting galaxies have too small and compact disks. More modern codes have included the effects of SN feedback, as it became clear that SNe strongly affect a number of galaxy properties such as the star formation activity, the triggering of mass-loaded winds, the amount of cold/dense gas fuel for star formation, and the angular momentum distribution of the baryons. However, the inclusion of SN feedback in simulations has been shown to be an extremely complex task, and a number of alternative approaches have been proposed in the last years (e.g. Springel & Hernquist 2003; Okamoto et al. 2005; Scannapieco et al. 2005, 2006; Rasera & Teyssier 2006; Stinson et al. 2006). Although these do not always give the exact same predictions for given dark matter haloes, many of them have shown to be successful in reproducing the formation of galaxy disks in a ΛCDM universe (e.g., Governato et al. 2004, 2007; Okamoto et al. 2005; Scannapieco et al. 2008, 2009; Ceverino & Klypin 2009; Stinson et al. 2010), overcoming the angular momentum problem.

In this work, I discuss current advances and challenges in the study of the formation of galaxies using hydrodynam-

⋆ Corresponding author: cscannapieco@aip.de

ical simulations in a cosmological context. First, I discuss the results of eight simulations of the formation of galaxies in a ΛCDM universe, with a variety of merger and accretion histories. In particular, I investigate how diverse simulated galaxies are, given that diversity must be a natural outcome of galaxy formation in ΛCDM.

A second topic of this paper focuses on the study of how realistic simulated galaxies are. This might seem an easy question; however, given that simulations and observations use very different techniques to analyse their results, it is hard to make a fair comparison and results might be misleading. In particular, I discuss how different estimations of galaxy structural parameters are – in particular disk-to-total ratios – when kinematic (as done in simulations) or photometric (as done in observations) decomposition techniques into bulge and disk are used.

Finally, I discuss the results of the Aquila Project (Scannapieco et al. 2012), that consists on the simulation of a unique initial condition of a Milky Way-mass galaxy using 13 different hydrodynamical codes. The main aim of the Aquila Project is to investigate the effects of feedback and numerical methods on the predictions of galaxy properties. The use of a unique initial condition, and an homogeneous set of analysis tools, allows to study the current state of simulations, in terms of their predictive power and robustness of the predictions.

This paper is organized as follows. Section 2 describes the simulation code and main characteristics of the two sets of simulations discussed in this paper. The first set is used to study the diversity of galaxies in ΛCDM (Sect. 3), the evolution of the galaxy morphology (Sect. 4), and the relation between kinematic and photometric disk-to-total ratios (Sect. 5). Section 6, where we use the second set of simulations, describes the Aquila Project and its main results. Finally, Sect. 7 summarizes the main conclusions of this work.

2 Methodology

In this work, we investigate three main subjects: (i) how similar or diverse are galaxies formed in ΛCDM, (ii) how simulated galaxies compare to observed ones, and (iii) how the predictions of different feedback models and numerical techniques compare, when a unique initial condition is used. For (i) and (ii), we use a set of eight simulations of Milky Way-mass galaxies, with great variety of formation and merger histories. In the case of (iii), we use the initial conditions of one of these eight galaxies, and run thirteen simulations using different numerical techniques (i.e., smoothed particle hydrodynamics (SPH), adaptive mesh refinement (AMR) and moving mesh) and different implementations of star formation and feedback.

In the rest of this Section, we discuss the main characteristics of these two sets of simulations.

Table 1 Main properties of our simulated halos at $z = 0$: virial mass, mass in stars, mass in gas and optical radius.

Halo	M_{200} (10^{11}M$_\odot$)	$M_{\rm star}$ (10^{10}M$_\odot$)	$M_{\rm gas}$ (10^{10}M$_\odot$)	$r_{\rm opt}$ (kpc)
Aq-A-5	14.9	9.0	4.6	17.9
Aq-B-5	7.1	4.0	1.7	17.7
Aq-C-5	16.1	10.8	3.6	16.0
Aq-D-5	14.9	7.9	3.2	14.8
Aq-E-5	10.8	8.4	2.6	10.6
Aq-F-5	9.1	7.7	1.7	14.1
Aq-G-5	6.8	4.4	1.53	14.1
Aq-H-5	7.4	6.5	0.52	10.4

2.1 Simulating various galaxies in ΛCDM

The first set of simulations comprises eight simulations, where the initial conditions correspond to galaxies with mass similar to the Milky Way, mildly isolated at $z = 0$, and with a variety of formation and merger histories. These simulations were first presented in Scannapieco et al. (2009), where we discussed the formation and survival of galaxy disks, and further analysis follows in Scannapieco et al. (2010, 2011), where we study the dynamical, structural and photometric properties of the simulated galaxies. Additional papers describe the effects of baryons on the dark matter distributions (Tissera et al. 2010) and the chemical patterns of simulated galaxies (Tissera, White & Scannapieco 2012).

The code we use for these simulations is described in in detail Scannapieco et al. (2005) and Scannapieco et al. (2006). The model includes stochastic star formation, metal-dependent cooling, a multiphase model for the gas component, chemical enrichment and feedback from Type II and Type Ia supernova. It is currently grafted onto GADGET3 (Springel et al. 2008), the most recent version of the Tree-PM SPH code GADGET (Springel 2005). The multiphase model is of particular importance since it allows hot, diffuse gas to coexist with a cold, dense gas phase (Scannapieco et al. 2006). This makes the deposition of SN energy into the interstellar medium more efficient, avoiding artificial losses usually occurring in standard SPH implementations of thermal feedback. We note that our star formation and feedback models are fully independent of those of Springel & Hernquist (2003) but we do use their treatment of a UV background, based on the work of Haardt & Madau (1996).

The initial conditions of this simulation series are based on those of the Aquarius Project (Springel et al. 2008). The eight target galaxies have been selected randomly from the parent dark-matter only simulation, the Millennium-II run (Boylan-Kolchin et al. 2009), with the only condition (additionally to the virial mass of the halo) of being mildly isolated (no neighbour exceeding half its mass within 1.4 Mpc). The simulations use the zoom-in technique, which allows to describe the formation of a galaxy and its surroundings with very high-resolution, keeping the information on the larger scales. This is done by using dif-

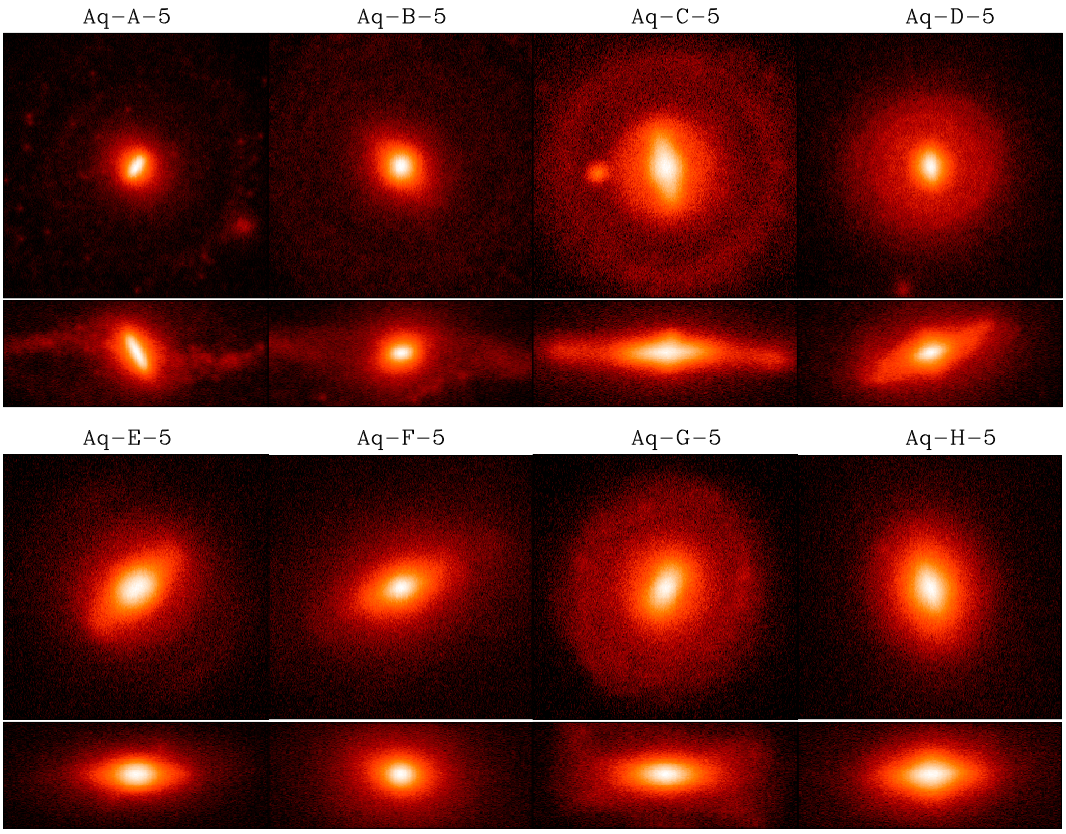

Fig. 1 Face-on and edge-on maps of projected stellar luminosity (i-band) for our simulations, at $z = 0$. The images are 50 kpc across, and the edge-on ones have a vertical height of 20 kpc (Scannapieco et al. 2010).

ferent hierarchies of particles whose mass resolution is decreased as they are further away from the target galaxy. Table 1 shows the virial masses, the masses in stars and gas, and the optical radii (the radius enclosing $83\,\%$ of the baryonic mass) of our simulated galaxies.

The simulations are consistent with a ΛCDM cosmology with $\Omega_\Lambda = 0.75$, $\Omega_\mathrm{m} = 0.25$, $\Omega_\mathrm{b} = 0.04$, $\sigma_8 = 0.9$ and $H_0 = 73\ \mathrm{km\,s^{-1}\,Mpc^{-1}}$. The eight simulations have similar dark matter and gas particle masses, of $\sim 10^6\ \mathrm{M_\odot}$ and $\sim 3\times10^5\ \mathrm{M_\odot}$, respectively. We have used similar gravitational softenings, either 0.7 or 1.4 kpc, which is the same for gas, stars and dark matter particles (see Scannapieco et al. 2009 for details).

2.2 Effects of numerical techniques and feedback models

The second set of simulations described in this paper correspond to those of the Aquila Project (Scannapieco et al. 2012). The Aquila Project aims at studying the effects of numerical techniques and feedback models on simulations of galaxy formation. The Aquila Project comprises thirteen simulations of a unique initial condition (that of Aq-C-5 of the previous subsection), using different codes. Most simulations use the smoothed particle hydrodynamics technique, some the adaptive mesh refinement technique and one uses the recently developed moving mesh technique (Springel 2010).

3 On the diversity of galaxies in ΛCDM

In a ΛCDM universe, galaxies are expected to be very different due to the great diversity of formation, accretion and merger histories. In this section, we use our set of eight simulations of Milky Way-mass galaxies, described in the previous section, to investigate how diverse simulated galaxies are. In particular, we study their morphologies, stellar populations, spatial structure and dynamics.

3.1 Galaxy morphology

Figure 1 shows maps of projected stellar luminosity in the i-band of the eight simulated galaxies (Scannapieco et al. 2010). It is clear that they have very different shapes and spatial extents, partly due to their different virial masses, but more importantly, due to their different formation and merger histories.

In order to quantify the morphology of the galaxies and to study the properties of disks and spheroids separately, we use a so-called kinematic disk-spheroid decomposition, that is based on the kinematics of the stars. As explained

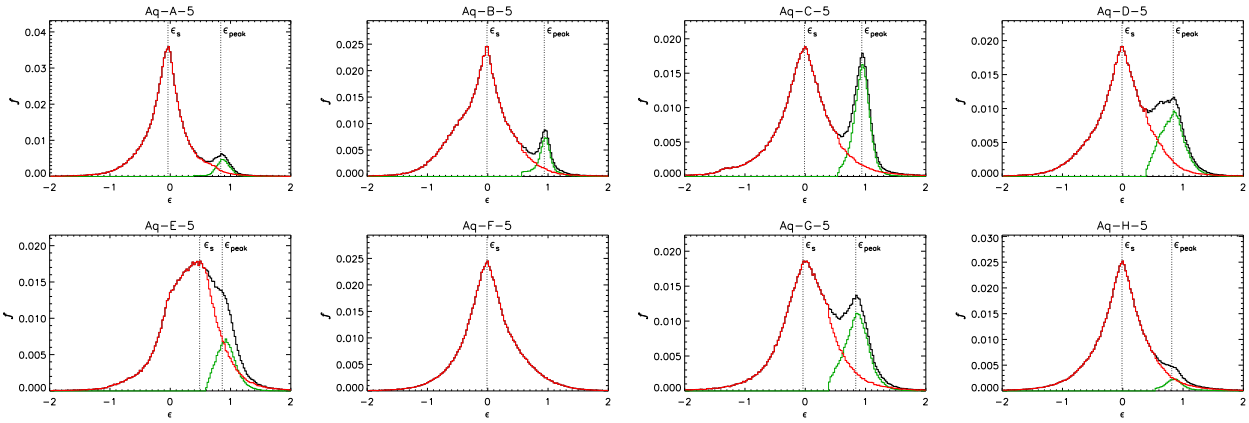

Fig. 2 Stellar mass fraction as a function of $\epsilon = j_z/j_{\rm circ}$ for our set of simulations at $z = 0$ (black lines). Red and green lines correspond to the distributions for spheroid and disk stars, respectively, obtained with our disk-spheroid decomposition (Scannapieco et al. 2009).

in Scannapieco et al. (2009), the decomposition is based on the definition of the stellar "circularities":

$$\epsilon \equiv j_z/j_{\rm circ}, \quad (1)$$

where j_z is the angular momentum of each star in the z direction (i.e. the direction of the total baryonic angular momentum) and $j_{\rm circ}$ is the angular momentum corresponding to a circular orbit at the position of the star. Stars with ϵ similar to unity, that identify stars with disk-like kinematics, are tagged as disk stars, while the remaining stars compose the spheroidal component. Note that spheroids then include bulge and stellar halo stars, but also stellar bars when these are present.

Figure 2 shows the distribution of stellar circularities of our simulations, and confirms the galaxy diversity already inferred from visual inspection of Fig. 1. Clearly, all galaxies show a significant spheroidal component, that, in all cases except for Aq-E-5, is not rotating, as indicated by the peak of the distribution at $\epsilon \sim 0$. On the other hand, all galaxies except for Aq-F-5 have disk components; however, the disk prominence varies significantly from galaxy to galaxy. In particular, four of the eight galaxies – Aq-C-5, Aq-D-5, Aq-E-5 and Aq-G-5 – have prominent disks. In contrast, Aq-A-5, Aq-B-5 and Aq-H-5 have very small disk components, and Aq-F-5 has no disk: this feature can be attributed to a recent major merger that fully destroys a pre-existing disk, as will be discussed in Sect. 4.

The kinematic disk-spheroid decomposition allows to calculate disk-to-total ratios for the simulated galaxies. Table 2 shows the (mass-weighted) disk-to-total ratios ($\rm D/T^k$) obtained with the kinematic approach. The maximum kinematic D/T ratios are about 0.2, and are too small to be compatible with disk-dominated galaxies. However, as we discuss in Sect. 5, when photometric bulge-disk decompositions are applied to the same simulated galaxies, the disk-to-total ratios vary significantly, making our results more compatible to observational results.

Table 2 Results from the kinematic and photometric decompositions of the eight simulated galaxies: we show the disk-to-total ratios obtained with the kinematic and photometric approaches, and the bulge-to-total and bar-to-total ratios of the latter method. Results in parenthesis correspond to galaxies for which the photometric decomposition did not give a reliable result.

Galaxy	$\rm D/T^k$	$\rm D/T^p$	$\rm B/T^p$	$\rm Bar/T^p$
Aq-A-5	0.06	0.32	0.45	0.23
Aq-B-5	0.09	0.42	0.58	–
Aq-C-5	0.21	0.49	0.28	0.23
Aq-D-5	0.20	0.68	0.32	–
Aq-E-5	0.14	0.40	0.17	0.43
Aq-F-5	–	(0.44)	(0.56)	–
Aq-G-5	0.23	0.60	0.06	0.34
Aq-H-5	0.04	(0.05)	(0.95)	–

3.2 Distribution of stellar ages

This Section describes the properties of simulated galaxies in terms of the age distributions of the disk and spheroid stellar populations. Because spheroid stars extend all the way to the virial radius (although the vast majority are in the central regions), we subdivide the spheroids into "inner" ($r \leq r_{\rm opt}$) and "outer" ($r > r_{\rm opt}$) components ($r_{\rm opt}$ is the radius which encloses $83\,\%$ of the baryonic galaxy mass, see Table 1).

Figure 3 shows the distribution of stellar ages for the disks, inner spheroids and outer spheroids, for our eight simulations. We find that, in all cases, the disks are the youngest components, while inner and outer spheroids are composed mainly of old stars. We find no systematic difference between the stellar age distributions of inner and outer spheroidal components. In the case of the disks, we find superposition of stars of different ages, perhaps indicative of thin and thick disks, as we discuss below.

Mean stellar ages are in the range 9–12 Gyr for spheroids and 4–9 Gyr for disks. These are mass-weighted

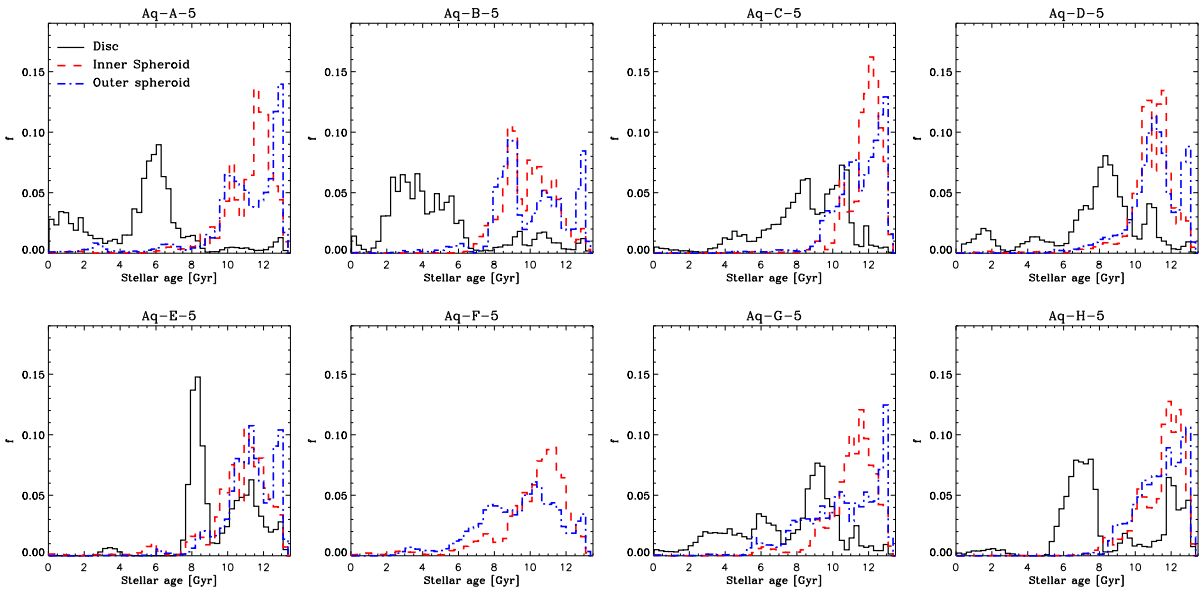

Fig. 3 Distribution of (mass-weighted) stellar ages for the disk (solid lines), inner spheroid (dashed lines) and outer spheroid (dotted-dashed lines) components in our simulations. For clarity, each component has been normalized to its total mass. From Scannapieco et al. (2011).

quantities, while in observations luminosity-weighted ages are obtained. We have calculated luminosity-weighted mean stellar ages for our simulations, using the Bruzual & Charlot (2003) population synthesis models. In this way, we obtain luminosity-weighted mean ages of 10–12 Gyr and 2–8 Gyr for the spheroids and disks, respectively. These values are very similar to the mass-weighted estimates for spheroids but, due to their younger ages, they are significantly lower for disks. The mean ages of our disks and spheroids are in relatively good agreement with observational results: observations find typical mean ages of bulges and disks of >8 Gyr and 4–12 Gyr, respectively (MacArthur et al. 2004, 2009).

The stellar age distributions can also be used to estimate the typical formation time-scales of the different components, simply from the values of the standard deviation. As is evident from Fig. 3, disks form over larger time-scales, with $\Delta\tau$ values between 2 and 3 Gyr. In contrast, the formation time-scales of spheroids are small, typically in the range 1–2 Gyr.

3.3 The structural and dynamical properties of simulated galaxies

We now discuss the structure of simulated disks and spheroids, in terms of spatial distribution and dynamical properties. Figure 4 shows the distribution of disk particles, in an edge-on view, of our simulations (note that Aq-F-5 has no disk). We plot separately stars formed in three different age bins: $t/\mathrm{Gyr} \leq 4$, $4 < t/\mathrm{Gyr} \leq 9$ and $t/\mathrm{Gyr} > 9$. The plots are color-coded according to the surface mass density at each point; covering 4 orders of magnitude (10^4–10^8 $\mathrm{M}_\odot$ kpc^{-2}).

We find that a few of the simulated disks are very thin (Aq-C-5, Aq-E-5) but we also detect a great variety: we find "boxy" or "X"-shaped disks (Aq-D-5, Aq-G-5, Aq-H-5), warps (Aq-B-5), and a case where two misaligned disks of different age are present (Aq-A-5). In all cases, however, we find that the youngest stars define thinner disks than stars in the older age bins.

Stars of different age also present different dynamical properties. As an example, we show in Fig. 5 the mean tangential velocity of disk stars as a function of projected radius for Aq-A-5, Aq-C-5 and Aq-E-5 and the corresponding velocity dispersion. (The results for the other runs are similar, see Scannapieco et al. 2011.) In all cases, the youngest components of the disks rotate ~ 2 times faster and have 2–3 times lower velocity dispersions than the older disk components. These results are indicative of the presence of young, thin components together with older and thicker disks; as also found in spiral galaxies.

Finally, we calculated the half-mass radii for simulated disks. As shown in Table 3, simulated discs have half-mass radii (r_d) that are consistent with observational results (see also Scannapieco et al. 2009, 2010).

Spheroids are also found to be very diverse, specially in their inner regions. Figure 6 shows maps of surface mass density for simulated inner spheroids (up to $0.5\times r_\mathrm{opt}$). Inner spheroids have bulge-like components that are very diverse in shape: some are almost axisymmetric, others are strongly ellipsoidal. Furthermore, some of the simulated galaxies, such as Aq-C-5 and Aq-G-5, have prominent bars (Scannapieco & Athanassoula 2012).

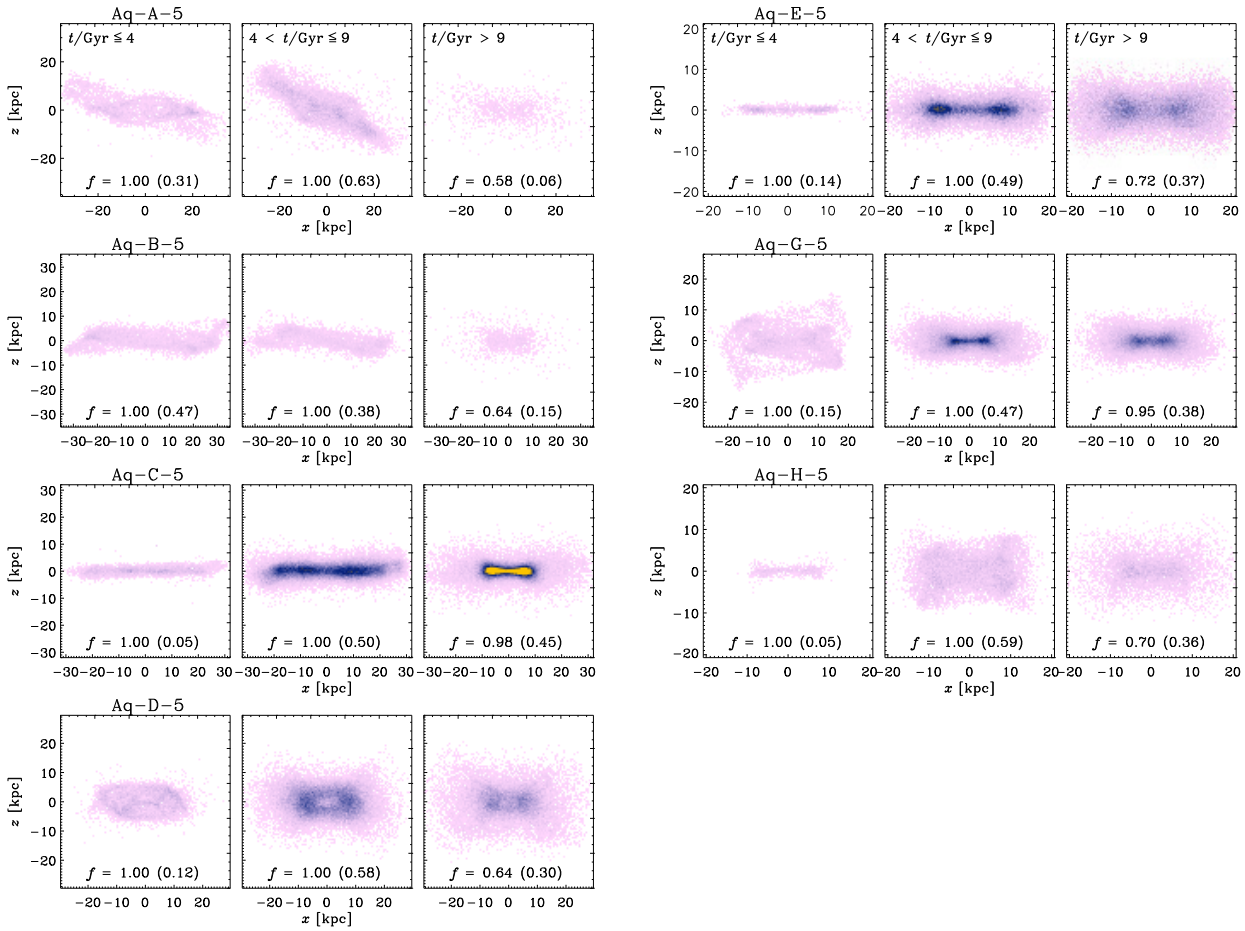

Fig. 4 Spatial distribution of disk particles (up to twice the corresponding optical radius) for the simulations with a disk component. We show separately the distribution of young stars ($t \leq 4$ Gyr), intermediate age stars (4 Gyr $< t \leq 9$ Gyr), and old stars ($t > 4$ Gyr) in the disks. Colours represent surface mass density, and cover 4 orders of magnitude (10^4–10^8 $M_\odot$ kpc^{-2}). We also show the in-situ fraction of disk stars for the three stellar age bins, together with the corresponding disk mass fraction (in parentheses). From Scannapieco et al. (2011).

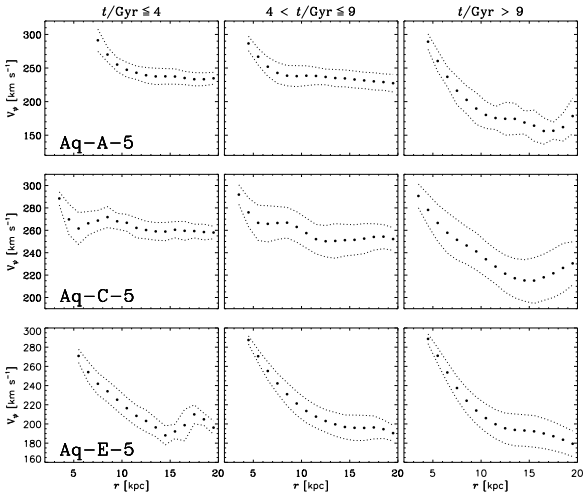

Fig. 5 Mean tangential velocity of disk stars as a function of projected radius in the disk plane (filled circles) for Aq-A-5, Aq-C-5 and Aq-E-5. The width between the dotted lines is the tangential velocity dispersion. From Scannapieco et al. (2011).

Table 3 Disc half-mass radii ($r_{\rm d}$) and best fit values for the inner and outer spheroid parameters: $\log \Sigma_{\rm eff}$, $r_{\rm eff}$, n (Sérsic law), and $\log \Sigma_{\rm o}$ and $r_{\rm o}$ (exponential). Units are kpc for $r_{\rm d}$, $r_{\rm eff}$ and $r_{\rm o}$, and $M_\odot$ kpc^{-2} for $\Sigma_{\rm eff}$ and $\Sigma_{\rm o}$. We also show the Q parameter used to test the goodness of the fits, as explained in the text.

Galaxy	$r_{\rm d}$	$\log \Sigma_{\rm eff}$	$r_{\rm eff}$	n	$\log \Sigma_{\rm o}$	$r_{\rm o}$	Q
Aq-A-5	21.2	9.1	1.5	2.5	7.1	12.1	0.008
Aq-B-5	24.0	8.6	1.8	2.7	7.1	10.6	0.012
Aq-C-5	12.2	8.9	2.3	1.2	7.4	10.3	0.003
Aq-D-5	11.0	8.8	1.9	2.5	7.4	10.3	0.009
Aq-E-5	12.9	8.8	2.5	1.2	7.1	12.3	0.016
Aq-F-5	–	8.5	2.8	1.7	7.5	10.5	0.006
Aq-G-5	10.8	8.6	2.2	1.5	7.0	8.1	0.008
Aq-H-5	10.6	8.6	2.6	1.3	7.6	6.9	0.005
Aq-C-6	8.2	8.6	2.6	1.0	7.3	8.9	0.012
Aq-E-6b	12.0	8.7	2.7	1.2	7.0	11.2	0.010
Aq-E-6	12.9	8.2	3.8	0.9	7.3	7.4	0.016

We have also constructed surface mass density profiles of the simulated spheroids (using equally-spaced bins in r), that are shown in Fig. 7. Note that we used stellar mass and not luminosity but, since these are old populations, very similar results are found in the two cases. The profiles were fitted using a combination of Sérsic and exponential profiles for the inner and outer regions, respectively, such that their sum gives the total surface mass density, namely:

$$\Sigma(r) = \Sigma_{\rm eff} \exp\left[-b_n\left(\left(\frac{r}{r_{\rm eff}}\right)^{\frac{1}{n}} - 1\right)\right] + \Sigma_{\rm o} \exp\left(\frac{r}{r_{\rm o}}\right).$$

The first term of the right-hand side in this equation is equivalent to the standard Sérsic law, i.e.,

$$\Sigma(r) = \Sigma_{\rm b} \exp\left[-\left(\frac{r}{r_{\rm b}}\right)^{\frac{1}{n}}\right],$$

but has the advantage that it can be expressed in terms of effective quantities usually quoted in observational studies (e.g. MacArthur et al. 2003). As explained in Scannapieco et al. (2011), we did additional tests replacing the exponential law used for the outer regions by either a power law or a Sérsic profile, but we found that, in general, the fits were poorer. Also, we repeated the fits changing the radius of the transition between the Sérsic and exponential laws. We estimated the goodness of the fits using the parameter Q:

$$Q \equiv \frac{1}{n}\sum_{i=1}^{n}(\log\Sigma_i - \log\Sigma_{i,\rm fit})^2,$$

where n is the number of data points; and, by minimizing Q, we selected the best-fit parameters. The results of the fits are shown in Table 3. In Fig. 7 we show the best-fit models (solid line) as well as the relative contributions of the Sérsic and exponential laws (dashed lines).

The inner spheroids ("bulges" if bars were absent) are characterized by central surface mass densities between $10^{8.5}$ and 10^{9} $\rm M_\odot\,kpc^{-2}$, and effective radii in the range 1.5–2.5 kpc. In terms of their shapes, the Sérsic parameters n are typically around 1, i.e., similar to exponential profiles. Aq-A-5 and Aq-B-5 have the highest n parameters, a reflection of their very concentrated profiles; on the contrary, Aq-H-5 has the lowest n value indicating a shallower profile in the central regions. The outer regions of the spheroids have much lower central surface densities, with $\Sigma_{\rm o} \sim 10^7$–10^8 $\rm M_\odot\,kpc^{-2}$, and scale-lengths of the order of 4–10 kpc. We find a wide range of relative contributions of the inner and outer components to the total spheroid mass, as can be clearly seen in Fig. 7. We note that, in the cases where bars are present, the profiles should perhaps include an additional component. This might explain the (small) differences between the results here and those presented in Scannapieco et al. (2010). However, we do not find larger Q values for galaxies with bars, suggesting that the number of fitting parameters is large enough to fit the 1D profiles of Fig. 7, even if bars are not included as an extra component.

Figure 8 shows the profiles of radial, tangential and vertical velocities for spheroid stars, as well as the corresponding total velocity dispersions. For the vertical velocities, we use $V_z^* \equiv V_z\ {\rm sign}(z)$, in order to distinguish between inflows ($V_z^* < 0$) and outflows ($V_z^* > 0$). We find very small radial and vertical velocity components in all simulations. In some cases, there are signs of non-zero but small radial velocities in the outermost regions, but these are not significant, specially taking into account that the amount of stellar mass in these regions is very small. We do find non-zero tangential velocities with a great variety of patterns: Aq-A-5 and Aq-B-5 are counter-rotating in the inner parts and co-rotating in the outer regions (always in relation to the overall rotation of the disk); the spheroidal component of Aq-E-5 has a net rotation (Scannapieco et al. 2009, 2011); the other galaxies show signs of co-rotation, mainly outside the inner regions. The total velocity dispersions decline with radius, varying typically from 150–250 km $\rm s^{-1}$ in the inner regions to 50–100 km $\rm s^{-1}$ near the virial radius.

The diversity in the structure and dynamics of galaxies arises naturally in our simulations, as a consequence of the variety of formation, merger and accretion histories in the context of the ΛCDM cosmological model.

4 Evolution of the galaxy morphology and relation to formation history

In this section, we discuss how the morphology of our eight simulated galaxies evolve, and which are the most important processes inducing morphological transformations. Figure 9 shows the evolution of the disk-to-total ratios (obtained using our kinematic method) for our eight simulations. Arrows indicate the entrance of satellites (see caption for color code), while the red points indicate periods of strong misalignment between the gas and stellar disks.

This figure nicely illustrates a number of features: (i) most galaxies have prominent disks at high redshift ($z \sim$ 2–3); (ii) the disk-to-total ratios significantly change between $z = 3$ and $z = 0$; (iii) the morphology of a galaxy can change in very short time-scales.

Major mergers are known to affect the morphology of galaxies; being able to convert disks into spheroids. In our eight galaxies, and between $z = 3$ and $z = 0$, we detect only one major merger event ($M_{\rm sat}/M_{\rm central} > 0.3$), that occurs in Aq-F-5 at $z \sim 0.5$. After the merger, the D/T ratio decreases from 0.3–0.4 to 0 very quickly, indicating that the merger fully destroyed the disk component.

Another possible mechanism to induce morphological transformations is a misalignment between the gas and stellar disks. We investigated this process and calculated the angle between the angular momentum of the pre-existing stellar disk and the angular momentum of the gas disk. In fact, we find a correlation between the alignment of infalling gas with respect to the stellar disk and the evolution of the D/T ratio. If infalling gas is misaligned with the stellar disks, the D/T ratios inevitably decrease, as indicated by the red

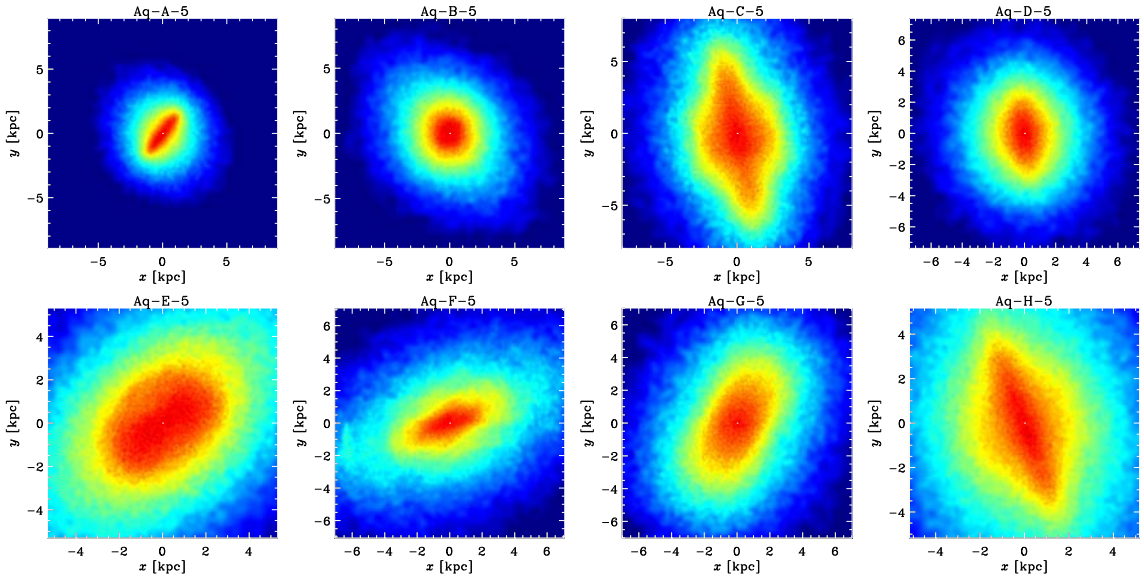

Fig. 6 Spatial structure of simulated inner spheroids, up to $0.5\,r_{\rm opt}$. The projection is face-on, such that the disks are contained in this plane. Colors represent projected surface mass density, on a logarithmic scale that covers 2.5 orders of magnitude. From Scannapieco et al. (2011).

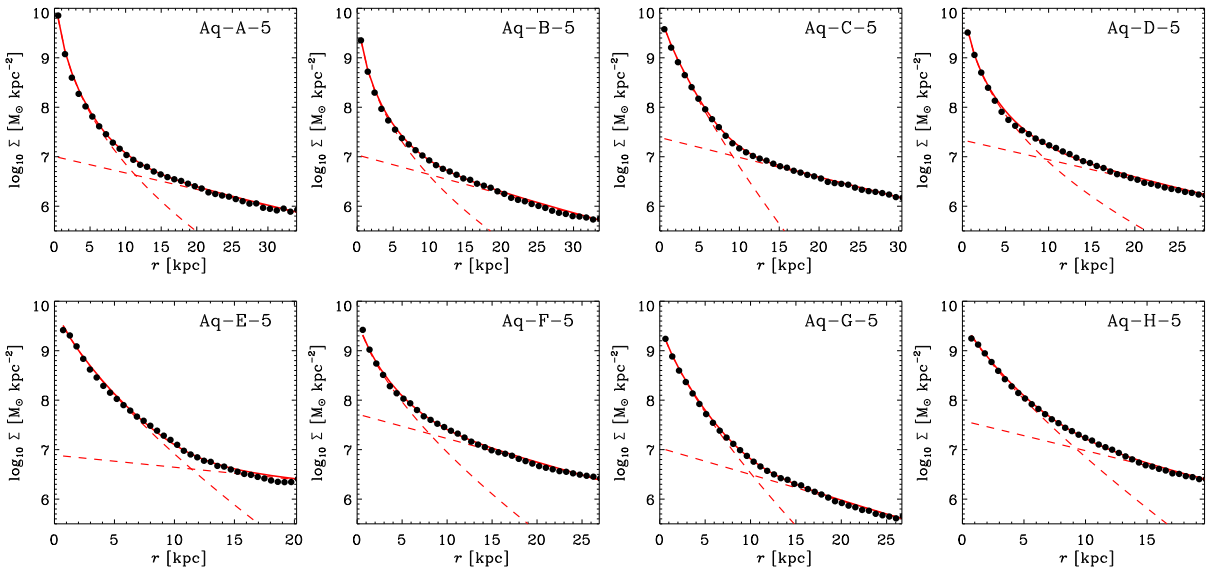

Fig. 7 Surface mass density profiles projected onto the disc plane (filled circles) for the spheroidal components of simulated galaxies (up to 2 times the corresponding optical radius). The solid lines show the best fit model assuming a Sérsic profile in the inner parts and a declining exponential law for the outer regions. The dashed lines show their relative contributions. From Scannapieco et al. (2011).

dots in Fig. 9. During these periods, disks become unstable: in some cases, such as Aq-A-5, Aq-B-5 and Aq-H-5, disks are almost completely destroyed; in others, disks survive (Aq-E-5). Note that the disk in Aq-A-5 was one of the most prominent disks of all simulations at $z \sim 1$; when the misalignment starts, the D/T ratio decreases from ~ 0.6 to 0.1. In Aq-D-5, the disk is destroyed but a new disk grows significantly at recent times.

Finally, we find that minor merger events can also affect disks, but their effects depend on other properties such as the satellite's orbit. In most cases of minor merger events, we find only little effects on the D/T ratios of simulated galaxies. However, in Aq-G-5, a minor merger is able to partially destroy the disk, lowering the D/T ratio from ~ 0.45 to 0.2 in a very short time.

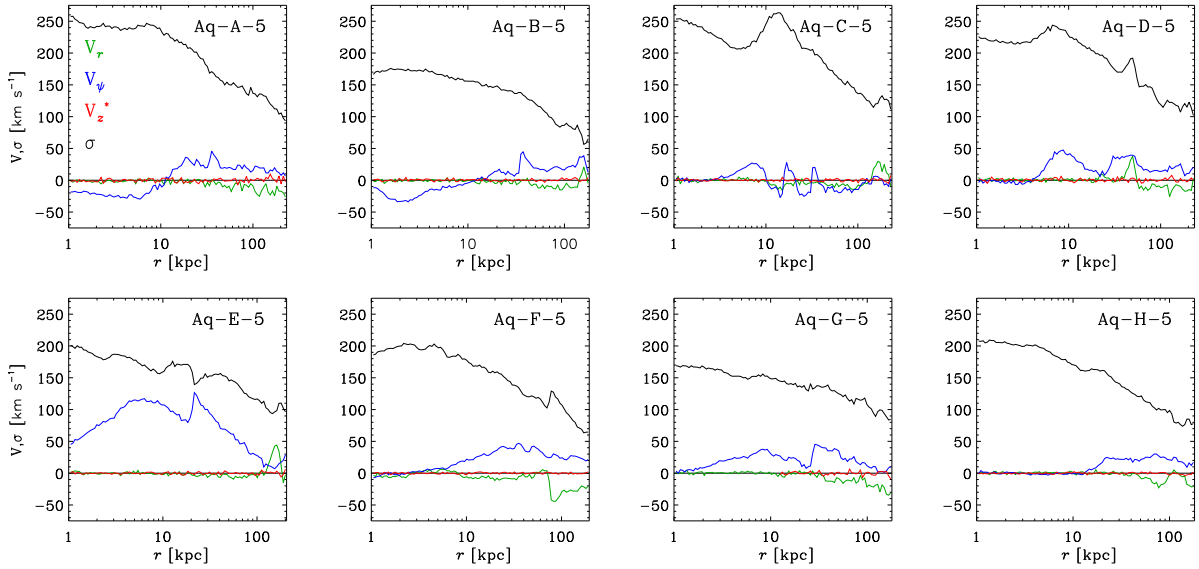

Fig. 8 Radial (green), tangential (blue) and vertical (red) velocities as a function of projected radius for the spheroidal components of our simulated galaxies (up to the corresponding virial radii). In the case of the vertical velocities, we use $V_z^* \equiv V_z\ \mathrm{sign}(z)$, in order to distinguish between inflows ($V_z^* < 0$) and outflows ($V_z^* > 0$). We also show the profiles of total stellar velocity dispersion (black lines). From Scannapieco et al. (2011).

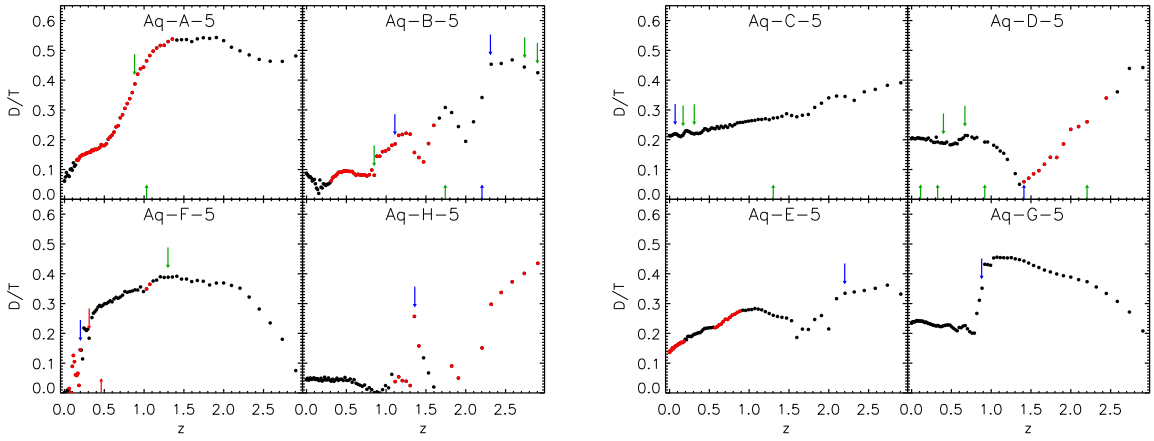

Fig. 9 Kinematic disk-to-total mass ratio as a function of redshift for simulated galaxies. We have divided the plot in such a way that galaxies with little or no disk components at $z = 0$ are plotted in the *left panel*, while galaxies with more prominent disks at the present time reside in the *right panel*. The arrows indicate the entrance of satellites either to the virial radius (upward arrows) or to the central (comoving) 27 kpc (downward arrows). Arrows are colour-coded according to the merger ratio $f \equiv M_{\rm sat}/M_{\rm cen}$: red, blue and green colours correspond to $f > 0.3$, $0.1 < f \leq 0.3$, and $0.02 < f \leq 0.1$, respectively. Red points indicate periods of strong misalignment between the cold gaseous and stellar disks. From Scannapieco et al. (2009).

5 Disk-bulge decompositions and the D/T ratio

As shown in Sect. 3.1, the disk-to-total ratios of simulated galaxies, obtained with a kinematic decomposition, are too small in comparison with disk-to-total ratios of spiral galaxies (Scannapieco et al. 2010; Stinson et al. 2010). It has been shown, however, that using different ways of segregating between disk and spheroidal components might lead to somewhat different results (e.g. Abadi et al. 2003; Governato et al. 2007).

Scannapieco et al. (2010) investigated whether the kinematic disk-spheroid decompositions usually used in simulation studies can be directly compared to the results of photometric decompositions, as done in real observations. To this end, we first produced synthetic images of the simulated galaxies using the radiative transfer code SUNRISE (Jonsson 2006). The images were then analysed using the BUDDA code (Gadotti 2008), that performs bulge-disk-bar

decompositions to observed images. The results of this photometric decomposition are shown in Table 2, where we list the disk-, bulge-, and bar-to-total ratios (D/T$^{\rm p}$, B/T$^{\rm p}$ and Bar/T$^{\rm p}$, respectively). Figure 10 shows the relation between the disk- and bulge-to-total ratios obtained kinematically and photometrically.

The disc-to-total ratios obtained from the kinematic and photometric decompositions differ significantly (Table 2 and Fig. 10). In most cases, the photometric D/T estimates are significantly higher than the kinematic ones. According to the kinematic decomposition, galaxies with significant disc components typically have D/T ~ 0.2 while the photometric decomposition yields estimates of 0.4–0.7. Moreover, for those galaxies with kinematically not very massive discs (D/T ≤ 0.09), the photometric estimates can be as high as ~ 0.4.

Although the kinematic decomposition estimates concern mass, while those from the photometric decomposition concern luminosity, this does not explain in this case such a discrepancy. As we have shown above, the mean stellar ages of the spheroid and disc components in the simulations are similar *and* they are both sufficiently old, meaning that differences in mass-to-light ratio between the different components are small. In fact, we find no significant difference when luminosity-weighted estimates (in the SDSS i band), calculated using the ages and metallicities of stars as inputs for the Bruzual & Charlot (2003) population synthesis models (for a Salpeter initial mass function as assumed in the simulations), are used (cf. open symbols in Fig. 10). Note that, in situations where disc and bulges have very different ages, this effect might however become important (e.g. Abadi et al. 2003). These results clearly indicate the importance of comparing simulations with observations in an appropriate manner. According to our results, estimates for D/T ratios obtained from a kinematic decomposition can be much lower than those obtained from photometry by observational methods.

Our results thus confirm that meaningful comparison between simulations and observations is crucial to identify agreement or disagreement between them; and that simply comparing kinematic and photometric disk-to-total ratios is probably not indicative of the similarity of simulated and observed galaxies.

6 The Aquila Project: a comparison of simulation codes

An important problem in hydrodynamical simulations of galaxy formation is that different simulation codes usually produce a variety of results. Although this is an important test for simulations, little effort has been invested in detailed comparisons of the predictions of different models and in understanding the origin of any differences. Moreover, due to the inhomogeneity of initial conditions, implementation techniques, included physics, selection of input parameters and analysis tools, it is impossible to compare the successes of different codes in an unbiased manner from published studies. The lack of systematic comparisons between models make it unclear how robustly galaxy properties can be predicted by hydrodynamical simulations in general.

The Aquila Project (Scannapieco et al. 2012) has been designed to overcome these problems. We used a unique initial condition (that of halo Aq-C of previous sections) and an homogeneous set of analysis tools, and simulated the formation of a single dark matter halo in a ΛCDM universe using 13 different codes.

The 13 various codes differ in their hydrodynamical technique: SPH, AMR and moving mesh. Among the 7 codes that use SPH, 6 are based on GADGET (hereafter G3 for short, (Springel 2005) and one on GASOLINE (hereafter referred to as GAS; Wadsley, Stadel & Quinn 2004). The three runs based on AMR correspond to the code RAMSES, and the moving-mesh code is the recently developed code AREPO. Each code was run by the group responsible for its development, adopting (independently from the choices made by other Aquila participants) their latest published model of cooling, star formation, and feedback. The main characteristics of each code are summarized in Table 4 (see Scannapieco et al. 2012 for more details).

In what follows, we summarize the main results of the Aquila Project, in relation to the galaxy morphologies, stellar masses, star formation rates and galaxy size.

6.1 Morphologies

Figure 11 shows face-on and edge-on maps of projected stellar mass for the thirteen simulations, at $z = 0$. The face-on projection is the one where the angular momentum of galaxy stars is perpendicular to the plotted plane. Visual inspection of these distributions show clear differences between the models. Some are more disky-like, others are spheroidal, and a few even show bars in their centers.

In order to better quantify the differences between models, we calculated the distribution of circularities, as defined in Sect. 3.1. The results are shown in Fig. 12, for the standard set of runs (with so-called level 5 resolution) and for the same runs at lower resolution (so-called level 6 resolution). This figure confirms that the galaxies produced by the thirteen codes are very different, and that the code-to-code variations in galaxy morphology are large.

6.2 Stellar masses

Figure 13 shows how the various implementations affect the stellar mass of the central galaxy, $M_{\rm stellar}$. This figure shows $M_{\rm stellar}$ as a function of $M_{200}(z)$, the virial mass of the main progenitor from $z = 2$ to $z = 0$. (The symbols correspond to values at $z = 0$.) We also show the total baryonic mass within the virial radius corresponding to the universal baryon fraction, $(\Omega_{\rm b}/\Omega_{\rm m})M_{200}$, which sets a hard upper limit to the stellar mass of the central galaxy (dashed line). The shaded region surrounding the dotted curve corresponds to the stellar masses predicted, at $z = 0$, by requiring

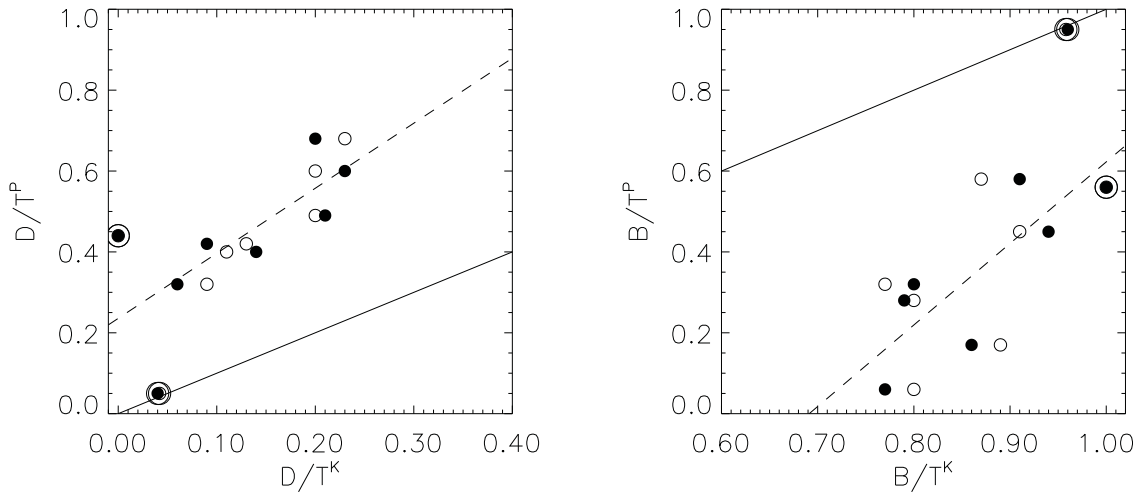

Fig. 10 Photometric versus kinematic results for the D/T and B/T ratios. In the case of the kinematic decomposition, we include mass-weighted (filled symbols) and luminosity-weighted (open symbols) estimates. The solid lines depict the one-to-one correspondence, and the dashed lines a linear fit to the data, excluding Aq-F-5 and Aq-H-5 (encircled symbols) for which the results of the photometric decomposition might not be reliable. The observed D/T in local late-type galaxies, with stellar masses similar to that of the Milky Way, ranges from about 0.7 to 1, while for B/T the corresponding value ranges from 0 to 0.2 (Gadotti 2009).

Table 4 Summary of code characteristics and sub-grid physics.

Code	Reference	Type	UV Background		Cooling	Feedback
			($z_{\rm UV}$)	(Spectrum)		
G3 (GADGET3)	(1)	SPH	6	(10)	Primordial (13)	SN (thermal)
G3-BH	(1)	SPH	6	(10)	Primordial (13)	SN (thermal), BH
G3-CR	(1)	SPH	6	(10)	Primordial (13)	SN (thermal), BH, CR
G3-CS	(2)	SPH	6	(10)	Metal-dependent (14)	SN (thermal)
G3-TO	(3)	SPH	9	(11)	Element-by-element (15)	SN (thermal + kinetic)
G3-GIMIC	(4)	SPH	9	(11)	Element-by-element (15)	SN (kinetic)
G3-MM	(5)	SPH	6	(10)	Primordial (13)	SN (thermal)
G3-CK	(6)	SPH	6	(10)	Metal-dependent (14)	SN (thermal)
GAS (GASOLINE)	(7)	SPH	10	(12)	Metal-dependent (16)	SN (thermal)
R (RAMSES)	(8)	AMR	12	(10)	Metal-dependent (14)	SN (thermal)
R-LSFE	(8)	AMR	12	(10)	Metal-dependent (14)	SN (thermal)
R-AGN	(8)	AMR	12	(10)	Metal-dependent (14)	SN (thermal), BH
AREPO	(9)	Moving Mesh	6	(10)	Primordial (13)	SN (thermal)

Notes: (1) Springel (2008); (2) Scannapieco et al. (2005, 2006); (3) Okamoto et al. (2010); (4) Crain et al. (2009); (5) Murante et al. (2010); (6) Kobayashi, Springel & White (2007); (7) Stinson et al. (2006); (8) Teyssier (2002); Rasera & Teyssier (2006); Dubois & Teyssier (2008); (9) Springel (2010); (10) Haardt & Madau (1996); (11) Haardt & Madau (2001); (12) Haardt & Madau (2005, priv. commun.); (13) Katz, Weinberg &Hernquist (1996); (14) Sutherland & Dopita (1993); (15) Wiersma et al. (2009); (16) Shen, Wadsley & Stinson (2010).

agreement between the halo mass and galaxy stellar mass functions through simple abundance matching (Guo et al. 2010). The prediction for Aq-C of the semi-analytic models GALFORM (Cooper et al. 2010) and L-GALAXIES (Guo et al. 2011) are also shown.

As we did for the galaxy morphology, we find significant differences in the predicted stellar mass for the thirteen codes, which varies between $\sim 4\times10^{10}\,{\rm M}_{\odot}$ and $\sim 3\times10^{11}\,{\rm M}_{\odot}$ at $z = 0$. The three largest stellar masses are obtained with the mesh-based codes, R, R-LSFE and AREPO, and correspond to assembling nearly all available baryons in the central galaxy. This illustrates the weak efficiency of the feedback implementations chosen for these codes, aided by the fact that, at comparable resolution, cooling efficiency is enhanced in mesh-based codes relative to SPH (e.g. Vogelsberger et al. 2011).

To understand whether the main cause of the differences can be attributed to the numerical technique, we can compare the results of G3 and AREPO, that use the exact same sub-grid physics and different numerical technique. We find that G3 forms only about half as many stars as AREPO. The galaxy formed by GAS also has a large stellar mass, but this

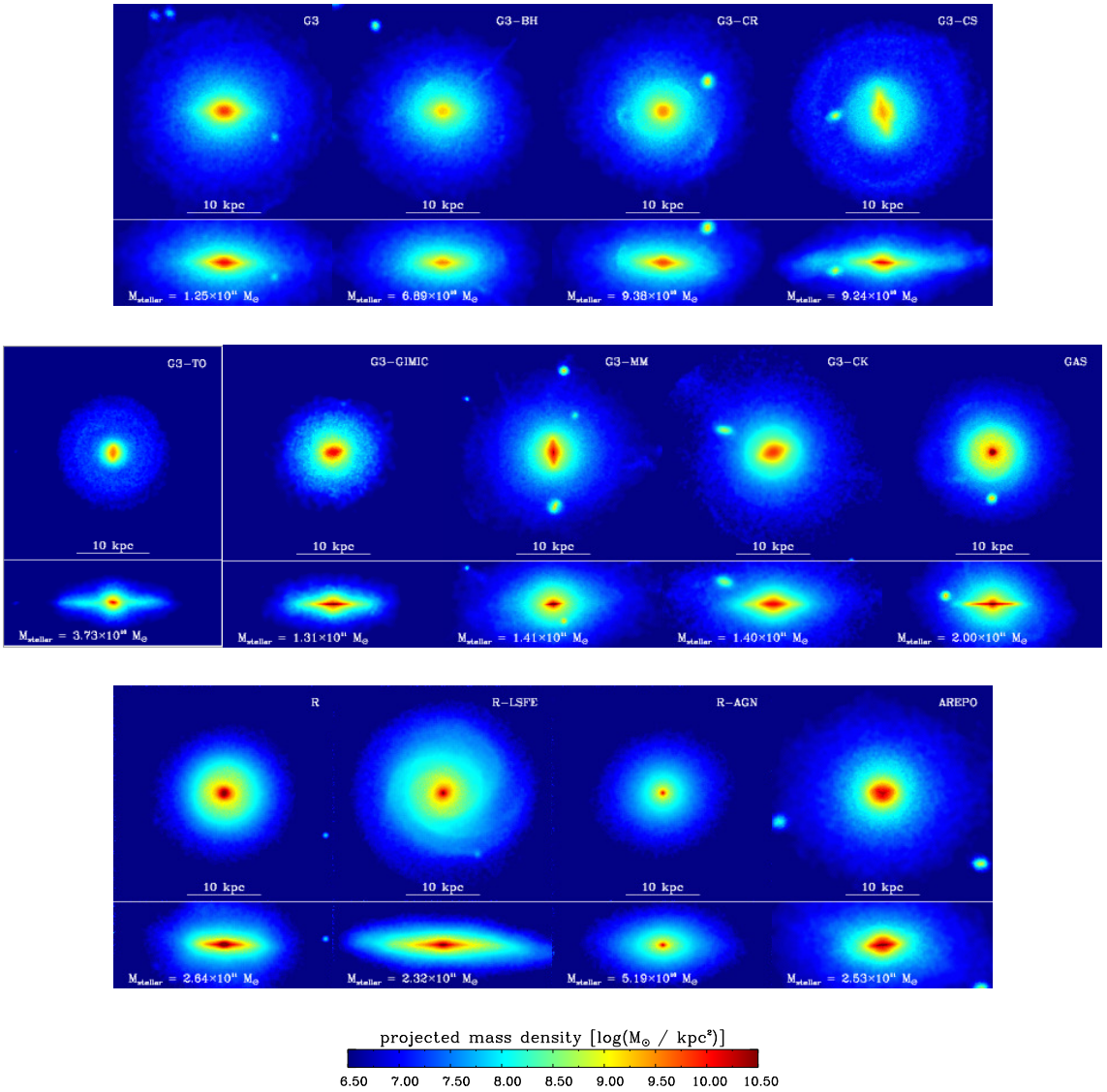

Fig. 11 Face-on and edge-on maps of projected stellar mass density. The face-on projection is along the direction of the angular momentum vector of galaxy stars. The face-on and edge-on maps are 30×30 kpc^2 and 30×12 kpc^2, respectively. The size of each pixel is 58.6 pc on a side and its color is drawn from a logarithmic color map of the surface stellar mass density. The total stellar mass within the galaxy radius ($r_{\rm gal} = 0.1\, r_{200} \sim 25$ kpc) is listed in the legend of each panel. From Scannapieco et al. (2012).

may be due to the fact that this code has a more efficient cooling function through the addition of metal-line cooling.

If we compare the results of codes that use the same numerical technique but different sub-grid physics, as is the case for all the G3-based codes, we detect even larger differences. Also for the three RAMSES codes, that have different sub-grid physics, we find large differences. In particular, when including AGN feedback in RAMSES, the stellar mass decreases by a factor of ~5 and the disk component is largely erased.

The results of this section show that, although the numerical technique may effect some changes in the stellar mass, these are small compared with the variations introduced by the feedback implementation.

6.3 Star formation rate

Figure 14 compares the present-day star formation rate (averaged over the past 0.5 Gyr to smooth out short-term fluctuations) with the stellar mass of simulated galaxies. We also show results from observations of nearby ($z < 0.1$) SDSS galaxies selected from the MPA-JHU DR7 catalog. The SFR of simulated galaxies varies from a low of ~0.02 M$_\odot$ yr^{-1} (R-AGN) to nearly 20 M$_\odot$ yr^{-1} (GAS), spanning the whole range covered by observed galaxies, from "red and dead" spheroids to actively star-forming gas-rich disks. The large scatter leads us to conclude that caution must be exercised when analyzing the instantaneous star formation rates of simulated galaxies, since these de-

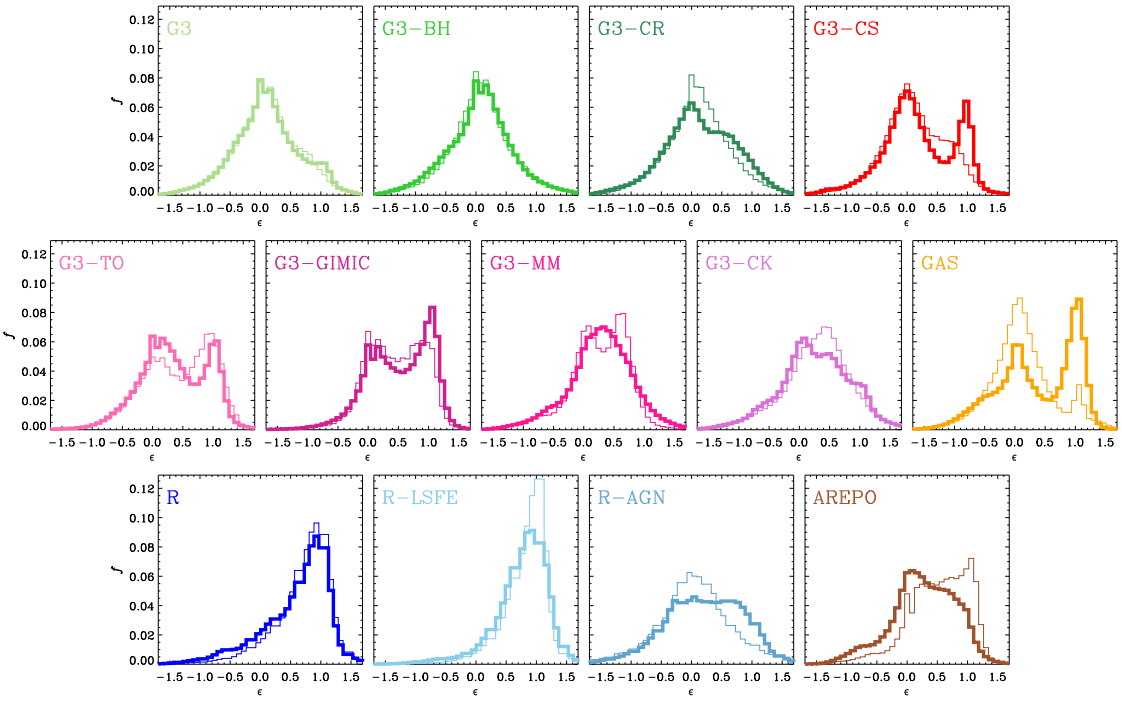

Fig. 12 Distribution of stellar circularities, $\epsilon = j_z/j_c$, for the different models. Thick and thin lines correspond to level-5 and level-6 resolution runs, respectively. From Scannapieco et al. (2012).

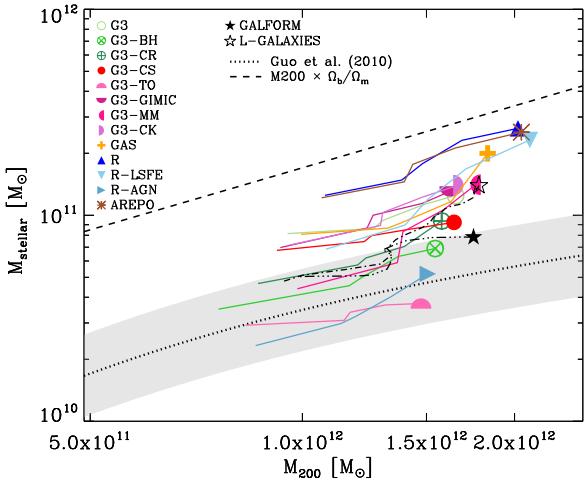

Fig. 13 The stellar mass of the central galaxy as a function of the virial mass of the surrounding halo. Curves of different color track the evolution of the galaxy in each simulation between $z = 2$ and $z = 0$. The dotted line indicates the stellar mass *expected* at $z = 0$ from the abundance-matching analysis of Guo et al. (2010); the shaded region corresponds to a 0.2 dex uncertainty. The dashed line indicates the mass of all baryons within the virial radius, $(\Omega_b/\Omega_m)\, M_{200}$. The filled and open star symbols indicate the predictions of the semi-analytic models GALFORM and L-GALAXIES for halo Aq-C, respectively. The dot-dashed curves show the evolution since $z = 2$ according to these two models.

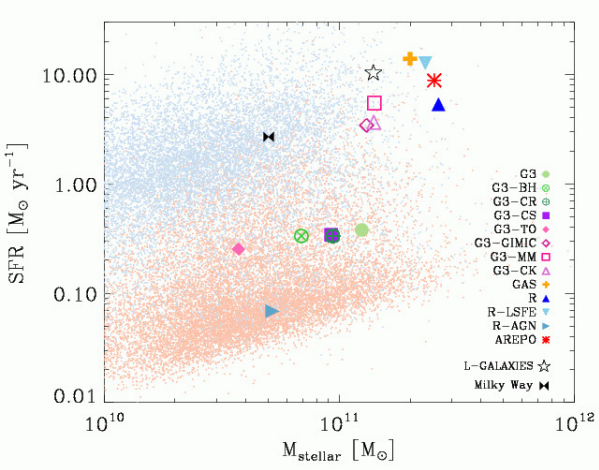

Fig. 14 Present-day star formation rate (averaged over the last 0.5 Gyr to smooth out short-term fluctuations) as a function of stellar mass. Blue and red dots correspond to a sample of nearby ($z < 0.1$) SDSS galaxies selected from the MPA-JHU DR7 catalog (only 5 percent of randomly selected data points are shown). The sample is split into "red sequence" and "blue cloud" galaxies as described in Fig. 15. We also show the prediction of the semi-analytic model L-GALAXIES of Guo et al. (2011) for Aq-C and the approximate location of the Milky Way. Note that the GALFORM semi-analytic model is not shown here since it predicts a present-day star formation rate close to zero. From Scannapieco et al. (2012).

pend sensitively on the details of accretion and of the implemented sub-grid physics.

6.4 Galaxy size

The left-hand panel of Fig. 15 shows the stellar half-mass radii of simulated galaxies. We also show the size of observed galaxies of similar stellar mass[1], the predictions of the GALFORM and L-GALAXIES semi-analytic models and the Milky Way, for reference. The observed sizes correspond to Petrosian half-light radii in the r-band rather than stellar half-mass radii so the comparison should only be taken as indicative.

We find that, in general, simulated galaxies are too compact to be consistent with typical spiral galaxies of comparable stellar mass. The more massive the simulated galaxy, the smaller its size, a trend that runs contrary to observation. The most massive simulated galaxies (R, R-LSFE, AREPO) are even smaller than most early-type galaxies, indicating that simulations where feedback is inefficient are not able to form disks with realistic sizes. In contrast, simulations where feeedback is more effective at curtailing the formation of stars give rise to galaxies with sizes in better agreement with observation.

The right-hand panel of Fig. 15 shows the projected half-mass radius of cold gas in the simulated galaxies (at $z = 0$) as a function of stellar mass and compares them with HI observations. The simulated gaseous disks are systematically more extended than the stellar component, in agreement with observation. They are also in better agreement overall with the typical size of H I disks, a result that suggests that material accreted relatively recently (and thus still in gaseous form) has, on average, enough angular momentum to form disks of realistic size. If feedback were able to favor the accretion and retention of this late-accreting, high-angular momentum gas, then simulated galaxies would have a much better chance of forming realistic disks.

6.5 Disks and formation time of stars

Although the 13 codes predict somewhat different stellar masses, galaxy sizes and star formation rates, we do find a correlation that gives us clues on the relation between the disk prominence and the formation time of the galaxy stars.

Figure 16 shows $f(\epsilon > 0.8)$, the fraction of stars with circularities larger than 0.8, versus the median formation time of all stars in the galaxy (expressed in terms of the expansion factor, $a_{50\%}$). The former gives a crude estimation of the importance of a thin disk. (Note, however, that these fractions often compare poorly with photometric estimates of the disk-to-total ratios as shown in Sect. 5.)

Figure 16 shows a clear correlation, where disks increase in prevalence in galaxies that make their stars later. On the other hand, galaxies that make their stars early tend to be spheroid-dominated. Only in four simulated galaxies do more than $\sim 40\,\%$ of stars have $f(\epsilon > 0.8) > 0.5$, two SPH-based and two AMR-based: R, R-LSFE, G3-GIMIC, and GAS. The most extreme case, R-LSFE, provides a clue to this behaviour. In this simulation feedback is inefficient and star formation is deliberately delayed, allowing gas to accrete into the galaxy and settle into a centrifugally-supported structure before turning into stars. Indeed, any mechanism that hinders the early transformation of gas into stars without curtailing gas accretion later on is expected to promote the formation of a disk (Navarro & Steinmetz 1997). As a result, the galaxies with most prominent disks are also the ones with the youngest stars (Agertz et al. 2011).

7 Conclusions

We have used two sets of simulations to highlight what are the current successes and challenges of galaxy formation simulations in a cosmological context.

We first used the Scannapieco et al. (2009) sample, that comprises eight galaxies similar in mass to our Milky Way and in a relatively quiet environment, and explored their $z = 0$ properties and the evolution in their morphologies. In particular, we investigated the degree of similarity and diversity of simulated galaxies. *We find that galaxies are very diverse, in terms of their structure, dynamical properties and stellar populations. This diversity arises naturally in the context of ΛCDM, where galaxies have very diverse accretion and merger history.*

The disks and bulges obtained in our simulations reproduce a number of properties that are observed in real galaxies: bulges are formed mainly by old stars, over short timescales, while disks are young and form over longer timescales. We also find that disks are better described by a superposition of more than one component: old disk stars rotate slower and have higher velocity dispersions than young disk stars. This result suggests the presence of thin and thick disk components in most simulated galaxies, similar to observational results.

We find that a *galaxy's morphology can significantly change during evolution, and this evolution is mainly driven by the particular merger and accretion history of the haloes. Additionally to major mergers that efficiently destroy disks, misalignment between the stellar disks and infalling gas strongly affects the disk-to-total ratios.* Such misalignments are common during galaxy formation, and are able to partially or fully destroy disks.

We have also compared estimations of the disk-to-total ratios obtained with photometric and kinematic disk-bulge decompositions. The former is used in observations, while the latter is the most common method used in simulation studies, given that simulations have information on the detailed dynamical state of a galaxy at any time. We found that *photometric disk-to-total ratios are systematically and significantly larger than kinematic ones*. While a kinematic decomposition gives maximum D/T ratios of the order of 0.2,

[1] Data taken from the SDSS MPA-JHU DR7 release for nearby ($z < 0.1$) galaxies; http://www.mpa-garching.mpg.de/SDSS/DR7/ .

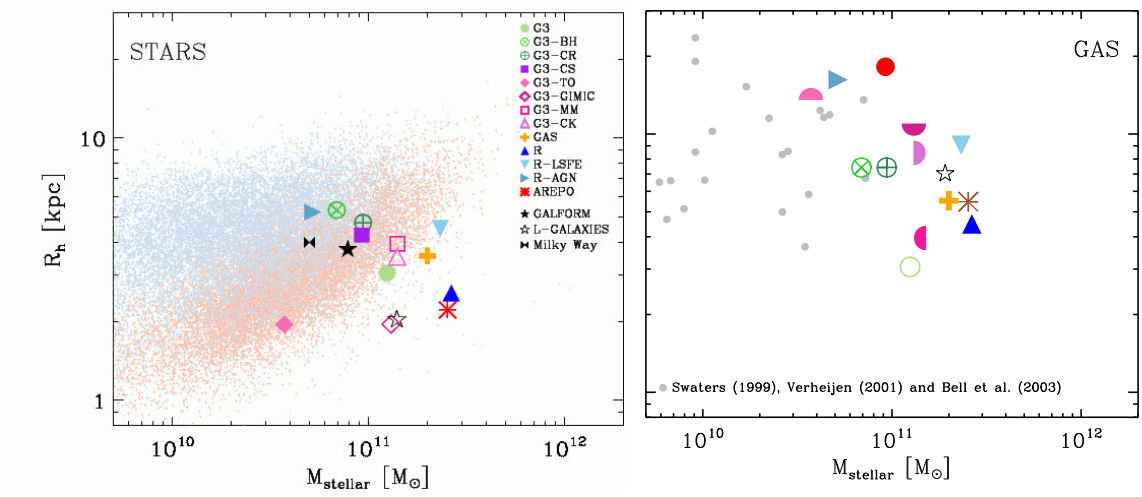

Fig. 15 *Left*: stellar half-mass radius as a function of the stellar mass of the galaxy. Blue and red dots show the Petrosian r-band half light radius for a sample of nearby ($z < 0.1$) SDSS galaxies taken from the MPA-JHU DR7 release. The sample is split into "blue cloud" and "red sequence" galaxies depending on their colors, according to the condition $(g-r) = 0.59+0.052\log(M_{\rm stellar}/M_\odot)-10.0$ (only 5 % of randomly selected data points are shown). We also show the predictions of the semi-analytic models GALFORM and L-GALAXIES for Aq-C, and the approximate location of the Milky Way in this plot. *Right*: The projected half-mass radius of cold ($T < 10^5$ K) gas in the galaxy as a function of stellar mass. Grey circles indicate the half-mass radii of H I disks compiled by Dutton et al. (2011) from Swaters et al. (1999) and Verheijen et al. (2001), and the open star symbol indicates the prediction of L-GALAXIES. The prediction of GALFORM is not shown here, since it predicts a present-day gas mass close to zero. From Scannapieco et al. (2012).

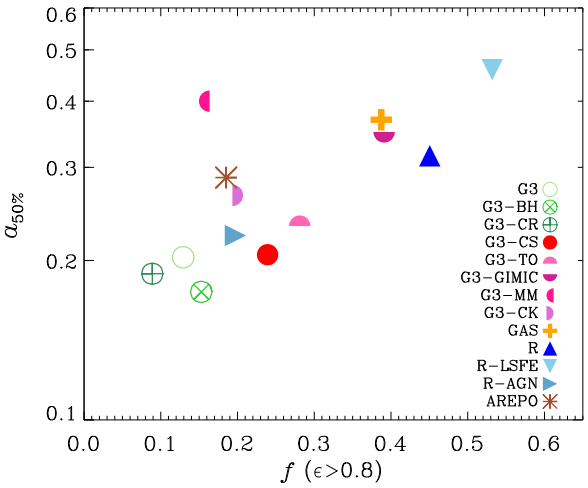

Fig. 16 Median formation time of stars in the galaxy at $z = 0$, expressed in terms of the expansion factor, $a_{50\%} = 1/(1+z_{50\%})$, as a function of the fraction of stars with circularity exceeding 0.8.

photometric methods yields values as large as 0.6 for the same galaxies. This means, on one side, that caution must be taken when using kinematic D/T ratios to test how realistic simulated galaxies are. On the other hand, our results indicate that photometric images might not be able to catch in detail the kinematical properties of a galaxy.

Finally, we have discussed the results of the Aquila Project, which compares the predictions of 13 different numerical codes for the properties of a galaxy in a Λ Cold Dark Matter universe. All simulations use a unique initial condition and are analysed in the exact same way, allowing a fair comparison of results. Despite the common halo assembly history, we find large ($\sim$1 dex) code-to-code variations in the stellar mass, size, morphology and star formation rate of the galaxy at $z = 0$. We investigated whether the differences can be attributed to the use of a different numerical technique (SPH, AMR, moving mesh), or to the use of different implementations of feedback processes. We found that the variations due to differences in the implementation of feedback are much larger than those induced by the use of a different numerical technique.

The Aquila Project has also revealed that feedback is a crucial mechanism in galaxy formation. Feedback self-regulates star formation, hindering the early transformation of gas into stars and, provided it does not curtail gas accretion later on, promotes the formation of a disk. As a result, the galaxies with most prominent disks are also the ones with the youngest stars.

At this point, it is clear that hydrodynamical simulations of galaxy formation in a cosmological context have allowed to understand many aspects of galaxy formation and evolution. The most important challenge now seems to be the description of star formation and feedback on a more physical basis. Given that cosmological simulations are still far from being able to resolve the small scales where these processes take place, the wisest way to go may be one where multiple numerical alternatives are developed and explored simultaneously and independently, provided that they are periodically contrasted in controlled experiments such as the Aquila Project.

References

Abadi, M. G., Navarro, J. F., Steinmetz, M., & Eke, V. R. 2003, ApJ, 597, 21
Agertz, O., Teyssier, R., & Moore, B. 2011, MNRAS, 410, 1391
Boylan-Kolchin, M., Springel, V., White, S. D. M., Jenkins, A., & Lemson G. 2009, MNRAS, 398, 1150
Bruzual, G., & Charlot, S. 2003, MNRAS, 344, 1000
Ceverino, D., & Klypin, A. 2009, ApJ, 695, 292
Cooper, A. P., Cole, S., Frenk, C. S., et al. 2010, MNRAS, 406, 744
Crain, R. A., Theuns, T., Dalla Vecchia, C., et al. 2009, MNRAS, 399, 1773
Dubois, Y., & Teyssier, R. 2008, A&A, 477, 79
Dutton, A. A., Conroy, C., van den Bosch, F. C., et al. 2011, MNRAS, 416, 322
Gadotti, D. A. 2008, MNRAS, 384, 420
Gadotti, D. A. 2009, MNRAS, 393, 1531
Governato, F., Mayer, L., Wadsley, J., et al. 2004, ApJ, 607, 688
Governato, F., Willman, B., Mayer, L., et al. 2007, MNRAS, 374, 1479
Guo, Q., White, S., Li, C., & Boylan-Kolchin, M. 2010, MNRAS, 404, 1111
Guo, Q., White, S., Boylan-Kolchin, M., et al. 2011, MNRAS, 413, 101
Haardt, F., & Madau, P. 1996, ApJ, 461, 20
Haardt, F., & Madau, P. 2001, Modelling the UV/X-Ray Cosmic Background with CUBA, in Clusters of Galaxies and the High Redshift Universe Observed in X-rays, ed. D. M. Neumann, & J. T. V. Tran, astro-ph/0106018
Jonsson, P. 2006, MNRAS, 372, 2
Katz, N., Weinberg, D. H., & Hernquist, L. 1996, ApJ, 105, 19
Kobayashi, C., Springel, V., & White, S. D. M. 2007, MNRAS, 376, 1465
MacArthur, L. A., Courteau, S., & Holtzman, J. A. 2003, ApJ, 582, 689
MacArthur, L. A., Courteau, S., Bell, E., & Holtzman, J. A. 2004, ApJS, 152, 175
MacArthur, L. A., González, J. J., & Courteau, S. 2009, MNRAS, 395, 28
Murante, G., Monaco, P., Giovalli, M., Borgani, S., & Diaferio A. 2010, MNRAS, 405, 1491
Navarro, J. F., & Steinmetz, M. 1997, ApJ, 478, 13
Okamoto, T., Eke, V. R., Frenk, C. S., & Jenkins, A. 2005, MNRAS, 363, 1299
Okamoto, T., Frenk, C. S., Jenkins, A., & Theuns, T. 2010, MNRAS, 406, 208
Rasera, Y., & Teyssier, R. 2006, A&A, 445, 1
Scannapieco, C., Tissera, P. B., White, S. D. M., & Springel, V. 2005, MNRAS, 364, 552
Scannapieco, C., Tissera, P. B., White, S. D. M., & Springel, V. 2006, MNRAS, 371, 1125
Scannapieco, C., Tissera, P. B., White, S. D. M., & Springel, V. 2008, MNRAS, 389, 1137
Scannapieco, C., White, S. D. M., Springel, V., & Tissera, P. B. 2009, MNRAS, 396, 696
Scannapieco, C., Gadotti, D. A., Jonsson, P., & White, S. D. M. 2010, MNRAS, 407, L41
Scannapieco, C., White, S. D. M., Springel, V., & Tissera, P. B. 2011, MNRAS, 417, 154
Scannapieco, C., & Athanassoula, E. 2012, MNRAS, 425, 10
Scannapieco, C., Wadepuhl, M., Parry, O. H., et al. 2012, MNRAS, 423, 1726
Shen, S., Wadsley, J., & Stinson, G. 2010, MNRAS, 407, 1581
Springel, V. 2005, MNRAS, 364, 1105
Springel, V. 2010, ARA&A, 48, 391
Springel, V., & Hernquist, L. 2003, MNRAS, 339, 289
Springel, V., Wang, J., Vogelsberger, M., et al. 2008, MNRAS, 391, 1685
Stinson, G., Seth, A., Katz, N., et al. 2006, MNRAS, 373, 1074
Stinson, G. S., Bailin, J., Couchman, H., et al. 2010, MNRAS, 408, 812
Sutherland, R. S., & Dopita, M. A. 1993, ApJS, 88, 253
Swaters, R. A., Schoenmakers, R. H. M., Sancisi, R., & van Albada, T. S. 1999, MNRAS, 304, 330
Teyssier, R. 2002, A&A, 385, 337
Tissera, P. B., White, S. D. M., Pedrosa, S., & Scannapieco, C. 2010, MNRAS, 406, 922
Tissera, P. B., White, S. D. M., & Scannapieco, C. 2012, MNRAS, 420, 255
Verheijen, M. A. W. 2001, ApJ, 563, 694
Wadsley, J. W., Stadel, J., & Quinn, T. 2004, New A, 9, 137
Wiersma, R. P. C., Schaye, J., & Smith, B. D. 2009, MNRAS, 393, 99

